

Regulating Polysulfide Transformation and Stabilizing Lithium Anode Using $[PMo_{12}O_{40}]^{3-}$ Cluster@Carbon Nanotube-Modified Separator for Lithium-Sulfur Batteries

He Zhou⁺,^[a] Zhiyuan Ma⁺,^[a] Guang Yang,^[a] Xinyuan Jiang,^[a] Suqing Duan,^[a] Yuchao Wu,^[a] Mengyao Wang,^[a] Lubin Ni,^{*[a]} Ligang Feng,^{*[a]} and Guowang Diao^{*[a]}

Lithium-sulfur (Li–S) batteries emerge as compelling contenders for next-generation energy-storage devices, boasting a noteworthy mass-specific energy of 2600 Wh kg⁻¹. However, the cycle stability and commercialization of Li–S batteries encounter challenges because of polysulfide shuttle and uncontrolled lithium dendrite growth. In this study, we present a polyoxometalates-based dual-function $[PMo_{12}O_{40}]^{3-}$ cluster@carbon nanotube modified polypropylene (PP) separator (PMo_{12} @CNT/PP) to regulate polysulfide transformation and safeguard the lithium anode in Li–S batteries. Leveraging its multi-electron redox properties and stable cluster structure, the PMo_{12} cluster acts as a polysulfide mediator, effectively capturing and

promoting electrochemical polysulfide transformation. The incorporation of CNT fosters consistent Li-ion nucleation, stabilizes the lithium anode, and impedes dendrite formation throughout cycling. Hence, Li–S cells equipped with the PMo_{12} @CNT/PP separator display higher capacity and better stability (675 mAh g⁻¹ at 3.0 C and 0.02% capacity decay per cycle over 700 cycles). The pouch cells with a sulfur loading 4.5 mg cm⁻² exhibit an initial discharge specific capacity of 925 mAh g⁻¹ at 0.1 C, and remain 849 mAh g⁻¹ after 40 cycles, underscoring the significant potential for practical applications of Li–S batteries.

Introduction

Lithium-sulfur (Li–S) batteries have garnered considerable attention owing to their high theoretical capacity (1675 mAh g⁻¹), environmental friendliness, nontoxicity, and low cost of sulfur.^[1–4] The theoretical energy density of Li–S batteries is 2600 Wh kg⁻¹, three to five times greater than that of commercial Li-ion batteries.^[5] Nevertheless, enduring challenges persist, rapid capacity fading, and the insulating property of sulfur, impeding electron/ion transfer. Additionally, the shuttle of lithium polysulfides (LiPSs) during charge/discharge processes results in low sulfur utilization and continuous threats from unrestrained lithium dendrites, significantly slowing their commercialization.^[6–10] In the multi-step discharge process, dissolved LiPSs diffuse from the cathode side to the anode side through the electrolyte due to different concentrations on either side of the separator.^[11–13] The shuttle effect damages Li–S batteries by reducing positive active material content and limiting sulfur utilization. The decrease in cycle stability and Coulomb efficiency results in a more pronounced self-

discharge.^[14,15] Separator properties play a crucial role in redox reaction kinetics and the interfacial behavior between electrodes and electrolytes. However, conventional polypropylene (PP) separators, with oversized pores, fail to effectively restrict the shuttle effect.^[16–18] The imperative need arises to design a functional separator capable of regulating polysulfide transformation and controlling dendrite growth. The distinctive characteristics of carbon materials, such as their expansive specific surface area, robust physical adsorption capacity, and exceptional mechanical strength, render them a compelling choice for the electrochemical field.^[19–27] Earlier investigations, involving the application of carbon films like carbon nanotube (CNT)^[28,29] and graphene oxide (GO)^[30,31] onto PP, have demonstrated efficacy in managing LiPSs. However, carbon materials cannot regulate the transformation of polysulfide. The incorporation of catalysts, including metal oxides,^[32] metal sulfides,^[33] MXenes,^[34] and MOFs,^[35] into the barrier separator is essential for capturing LiPSs and accelerating their transformation to Li_2S_2/Li_2S by enhancing redox kinetics.

Polyoxometalates (POMs) represent a category of metal-oxygen cluster compounds, predominantly composed of cations and polyanions, with preferred elements being Mo, W, V, Nb, and Ta. These compounds exhibit an impressive open nanocluster structure, multi-electron redox properties, and stability in their cluster structure throughout reduction-oxidation processes. These characteristics make them highly promising for a range of applications in various catalytic reactions^[36–37] and electrocatalysis,^[38–39] and other electrochemical reactions.^[40–58] In 2018, Dong, Cronin, and their co-workers developed a dual-function Lewis acid and base catalyst for Li–S batteries in the form of an Ag(I)-substituted Keggin

[a] H. Zhou,⁺ Z. Ma,⁺ G. Yang, X. Jiang, S. Duan, Y. Wu, M. Wang, L. Ni, L. Feng, G. Diao

School of Chemistry & Chemical Engineering

Yangzhou University

Yangzhou 225002, Jiangsu, People's Republic of China

E-mail: Ibni@yzu.edu.cn

fenglg11@gmail.com

gwdiao@yzu.edu.cn

[+] These authors contributed equally

Supporting information for this article is available on the WWW under <https://doi.org/10.1002/batt.202300563>

$K_3[H_3AgIPW_{11}O_{39}]$ cluster. LiPSs can be strongly adsorbed on the $\{AgIPW_{11}O_{39}\}$ cluster. This interaction serves to enhance the chemical affinity between LiPSs and the POMs.^[59] Then, Wei, Diao, Ni, and their co-workers introduced a POMs-based sulfur host material incorporating a Keggin-type $H_3PW_{12}O_{40}$ embedded into a 3D reduced graphene oxide-CNT (rGO-CNT) conductive matrix. $H_3PW_{12}O_{40}$ catalyzed the reduction of long-chain LiPSs (Li_2S_n , $4 \leq n \leq 8$) and the oxidation of short-chain LiPSs(Li_2S_2/Li_2S), thus enhancing the redox kinetics of Li–S batteries. However, $H_3PW_{12}O_{40}$ experienced partial lithiation, increasing its solubility in electrolytes and consequently leading to the loss of the catalyst.^[60] To tackle this challenge, Chen, Dong, and co-workers designed an innovative composite by combining POMs with rGO, forming a bifunctional electrocatalyst in 2022. This novel POMs/rGO composite utilized a positively charged polymer to link $[Co_4(H_2O)_2(PW_9O_{34})_2]^{10-}$ clusters to the rGO. The exposed unsaturated cobalt (Co) atoms within $[Co_4(H_2O)_2(PW_9O_{34})_2]^{10-}$ clusters played a pivotal role, enhancing the adsorption of LiPSs and concurrently lowering the activation energy associated with the conversion of LiPSs.^[61] Although the use of POMs-based composites as sulfur hosts increased polarization due to the poor conductivity of POMs, it acted as a bidirectional molecular catalyst and accelerated interfacial charge transfer. Other studies focused on modifying commercial PP separators using POMs. In 2018, Su, Qin, and their collaborators innovatively crafted a bifunctional composite separator, $[PW_{12}O_{40}]^{3-}$ /Super P, strategically harnessing Coulombic repulsion between $[PW_{12}O_{40}]^{3-}$ and LiPSs to effectively hinder the shuttle effect.^[62] Recently, Diao, Wei, Ni, and their collaborators introduced an innovative crystalline material, comprising $[Zn_2(H_2O)_3](WO_2)_2(SbW_9O_{33})_2]^{10-}$ and two β -cyclodextrin ($Zn_2W_2@2CD$), for the modification of the separator in Li–S batteries. It has been demonstrated that POMs exhibit a bidirectional catalytic effect on LiPSs. Additionally, the distinctive structure of CD facilitates the transport channel for Li-ions. This molecular-level assembly facilitates the controlled immobilization of POM and effectively captures LiPSs.^[63] While the aforementioned research has delved into understanding the

catalytic mechanism of POMs and successfully addressed the issue of POMs loss, as well as effectively mitigated the shuttle effect, the persistent challenge of dendrite formation remains unresolved.

In this work, we present a bifunctional separator utilizing a Keggin-type $[PMo_{12}O_{40}]^{3-}$ cluster@CNT modified PP separator ($PMo_{12}@CNT/PP$) for Li–S batteries, effectively curtailing the shuttle of polysulfides and impeding the growth of lithium dendrites (Figure 1). The $[PMo_{12}O_{40}]^{3-}$ cluster, bearing a negative charge, electrostatically interacts with CNT coated with positively charged conducting polymer (TBA) ultra-thin layers. The PMo_{12} cluster, with its bi-directional catalytic performance, facilitates the conversion of long-chain LiPSs to short-chain LiPSs during discharging and actively catalyzes the production of long-chain LiPSs during charging. Additionally, the CNT enhances the swift transfer of Li-ion and exhibits excellent physical adsorption to LiPSs. The utilization of the $PMo_{12}@CNT/PP$ separator in Li–S batteries resulted in commendable rate performance and stability (675 mAh g⁻¹ at 3.0 C and 0.02% capacity decay per cycle over 700 cycles). The pouch cell underwent cycling at a sulfur load of 4.5 mg cm⁻², achieving a discharge-specific capacity of 925 mAh g⁻¹. Even after 40 cycles, the battery retained a substantial capacity of 849 mAh g⁻¹. Continued investigation and optimization of POMs integration into Li–S batteries hold great promise for enhancing overall performance, reliability, and battery lifespan.

Results and Discussion

Scanning Electron Microscopy (SEM), High-resolution Transmission electron microscopy (HRTEM), and high-angle annular dark-field scanning transmission electron microscope (HAADF-STEM) were applied to scope the structure and morphology of PP, and the $PMo_{12}@CNT/PP$ separator. The SEM image illustrates the flat surface of a conventional PP separator (Figure 2a). While the PP separator facilitates Li-ion diffusion channels, it fails to impede the shuttling of polysulfides, resulting in continual

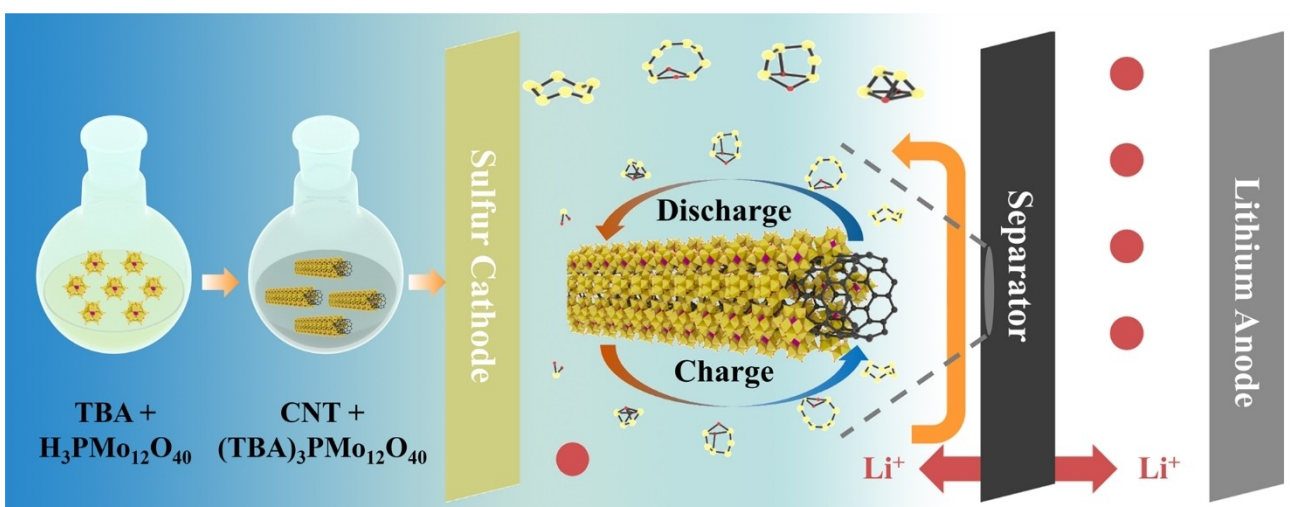


Figure 1. Schematic illustration of the fabrication of functional $PMo_{12}@CNT/PP$.

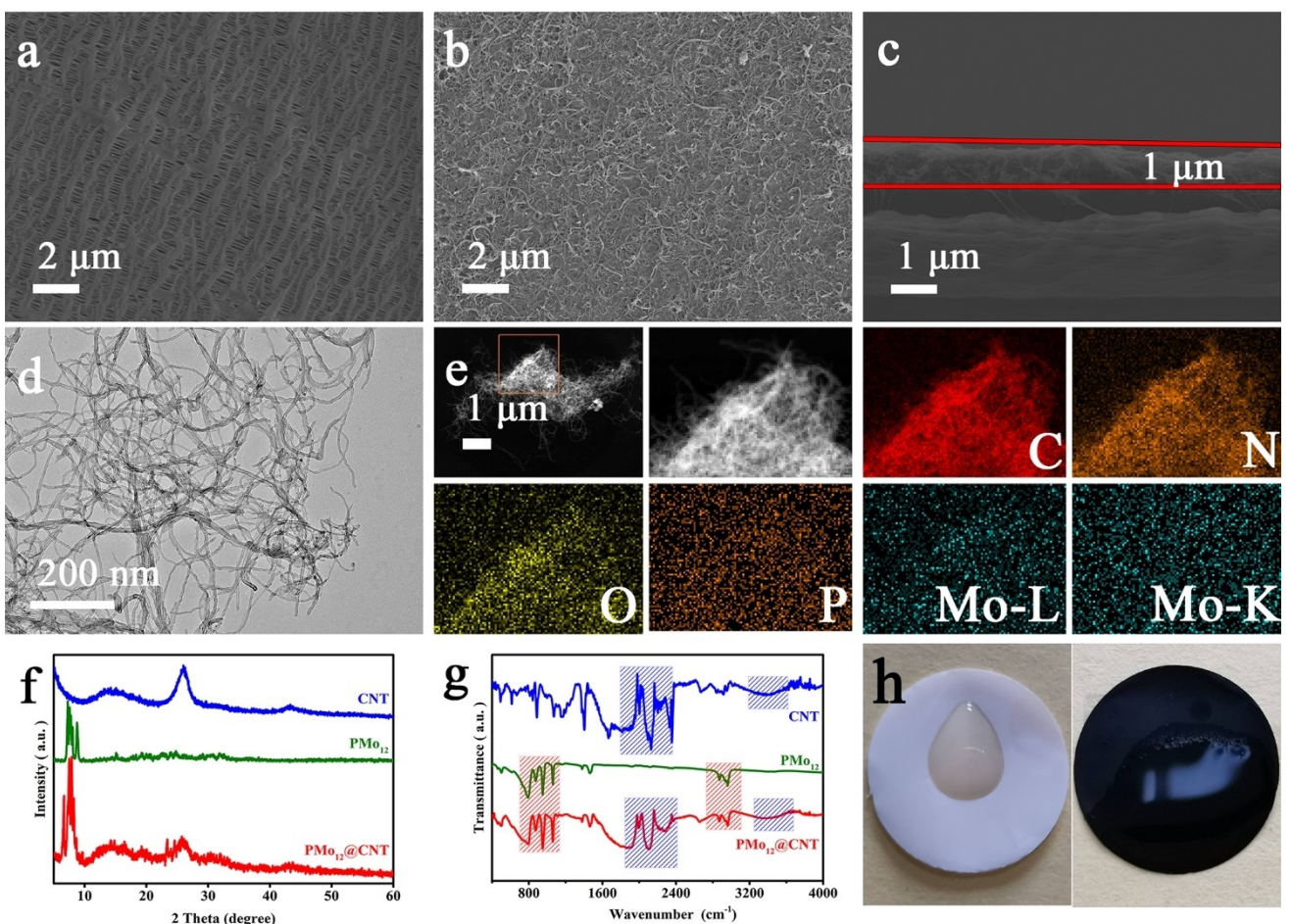


Figure 2. Top-view SEM images of a) PP and b) PMo₁₂@CNT/PP separator. c) Cross-section SEM image of PMo₁₂@CNT/PP separator. d) TEM and e) STEM image and EDX elemental mapping images of PMo₁₂@CNT. f) XRD patterns of CNT, PMo₁₂, and PMo₁₂@CNT. g) FT-IR spectra of CNT, PMo₁₂, and PMo₁₂@CNT. h) Contact angle measurements with the electrolyte for PP and PMo₁₂@CNT/PP separator.

sulfur loss and a decline in battery life. Figure 2b shows that the incorporation of PMo₁₂@CNT into the PP separator eradicates visible macropores in the resulting composite separator. To corroborate this, Brunauer-Emmett-Teller analysis (BET) was employed to characterize the surface state of PP and PMo₁₂@CNT/PP separator. The PMo₁₂@CNT effectively covers the large pores in the PP separator, providing a hindrance to the passage of LiPSs while ensuring the migration of Li-ion. The incorporation of CNT amplifies the adsorption capacity of the PMo₁₂@CNT/PP separator, thereby strengthening its affinity to LiPSs. The surface area of PMo₁₂@CNT/PP is 46.072 m² g⁻¹, while PP is 59.650 m² g⁻¹ (Figure S1a and Figure S1b). In Figure 2c, a cross-sectional view of the composite separator reveals an approximately 1 μm loading of PMo₁₂@CNT on PP. Although the Thermogravimetric Analysis (TGA) reveals a PMo₁₂ cluster content as high as 20.5% in PMo₁₂@CNT (Figure S2), their small size prevents substantial aggregation, as evidenced by transmission electron microscope images (Figure 2d). Energy-dispersive X-ray Spectrometer (EDX) elemental mapping of C, N, O, P, and Mo in Figure 2e distinctly illustrates the even dispersion of the PMo₁₂ cluster on the surface of the CNT.

The crystallinity and composition of the PMo₁₂ cluster, CNT, and PMo₁₂@CNT were analyzed using Powder X-ray diffraction (PXRD) (Figure 2f). On the PMo₁₂@CNT curve, a distinct peak at 26.6°, attributed to the (002) crystallographic planes of CNT, is observable.^[64] Characteristic peaks of the PMo₁₂ cluster around 10° are also discernible in the PMo₁₂@CNT curve.^[65] Fourier Transform Infrared (FT-IR) spectra (Figure 2g) of PMo₁₂@CNT reveal four distinctive absorption peaks at 1069, 953, 871, and 789 cm⁻¹. These peaks belong to the bending vibration of P–O, the anti-symmetric telescopic vibration of Mo=O_d, the telescopic vibration of Mo–O_c–Mo, and the telescopic vibration of Mo–O_b–Mo, respectively, in the PMo₁₂ cluster.^[66] The Raman spectra of CNT, PMo₁₂ cluster, and PMo₁₂@CNT are presented in Figure S3. The peak around 1000 cm⁻¹ belongs to the PMo₁₂ cluster. Two typical peaks, D peak (around 1360 cm⁻¹) and G peak (around 1560 cm⁻¹) occur at CNT and PMo₁₂@CNT curves. The I_D/I_G value increases from 0.766 for CNT to 1.002 for PMo₁₂@CNT, indicating the removal of functional groups and the formation of defects resulting from the partial reduction of CNT. In contrast to pure PP, the PMo₁₂@CNT/PP separator exhibits improved wettability with electrolyte and lower surface tension (Figure 2h), facilitating enhanced Li-ion flow and trans-

fer. To explore the adsorption capacity of $\text{PMo}_{12}\text{@CNT}$ for LiPSs, a predetermined quantity of $\text{PMo}_{12}\text{@CNT}$ was introduced into a Li_2S_4 solution (Figure 3a). After reacting for 0.5 h, the solution became nearly colorless and transparent, indicating the robust adsorption capability of $\text{PMo}_{12}\text{@CNT}$ for Li_2S_4 . UV-visible spectrophotometry (UV) analysis of the sample liquid, after the 0.5 h treatment, revealed a prominent absorption peak at 417 nm in the blank Li_2S_4 solution. Contrastingly, the Li_2S_4 solution with added $\text{PMo}_{12}\text{@CNT}$ exhibited no discernible absorption peaks, affirming the vigorous adsorption capacity of $\text{PMo}_{12}\text{@CNT}$ for Li_2S_4 . For a more profound understanding of the interaction mechanism between the PMo_{12} cluster and LiPSs, X-ray photo-electron spectroscopy analysis (XPS) was employed. The Mo 3d_{3/2} spectrum of the pristine PMo_{12} cluster displayed characteristic double peaks at 236.2 eV and 233.1 eV, consistent with Mo^{6+} . After a 0.5 h Li_2S_4 treatment, Mo^{6+} underwent reduction to Mo^{5+} , leading to a Mo 3d spectrum with relative concentrations of 66.8% for Mo^{6+} and 33.2% for Mo^{5+} (Figure 3b).^[67] Simultaneously, the S 2p XPS spectrum of pristine Li_2S_4 (Figure 3c) exhibited double peaks at 163.2 eV and 161.7 eV,

corresponding to bridging sulfur (S^0) and terminal sulfur (S^{-1}). Following a 0.5 h treatment with the PMo_{12} cluster, the S 2p spectrum revealed three distinct sulfur states, indicating redox interactions with polysulfides. The oxidation process of Li_2S_4 induced by its reaction with the PMo_{12} cluster led to the formation of polythionate and thiosulfate, accompanied by the conversion of Mo^{6+} to Mo^{5+} . These findings affirm a robust interaction between the PMo_{12} cluster and LiPSs.^[68] To better understand the reduced PMo_{12} cluster species, a visual beaker battery equipped with a $\text{PMo}_{12}\text{@CNT}$ electrode in a Li-S electrolyte was conducted, as illustrated in Figure S4a. Throughout the initial discharge cycle, the electrolyte in the beaker battery undergoes a transition from its initial transparency to a dark blue color. The UV vis spectra of the electrolyte reveal a prominent absorption band at 760 nm, signifying the gradual reduction of the PMo_{12} cluster to heteropoly blue, as depicted in Figure S4b.

To estimate the effectiveness of the $\text{PMo}_{12}\text{@CNT}/\text{PP}$ separator in regulating polysulfide transformation, H-type glass cells were utilized to assess the permeation of LiPSs under different

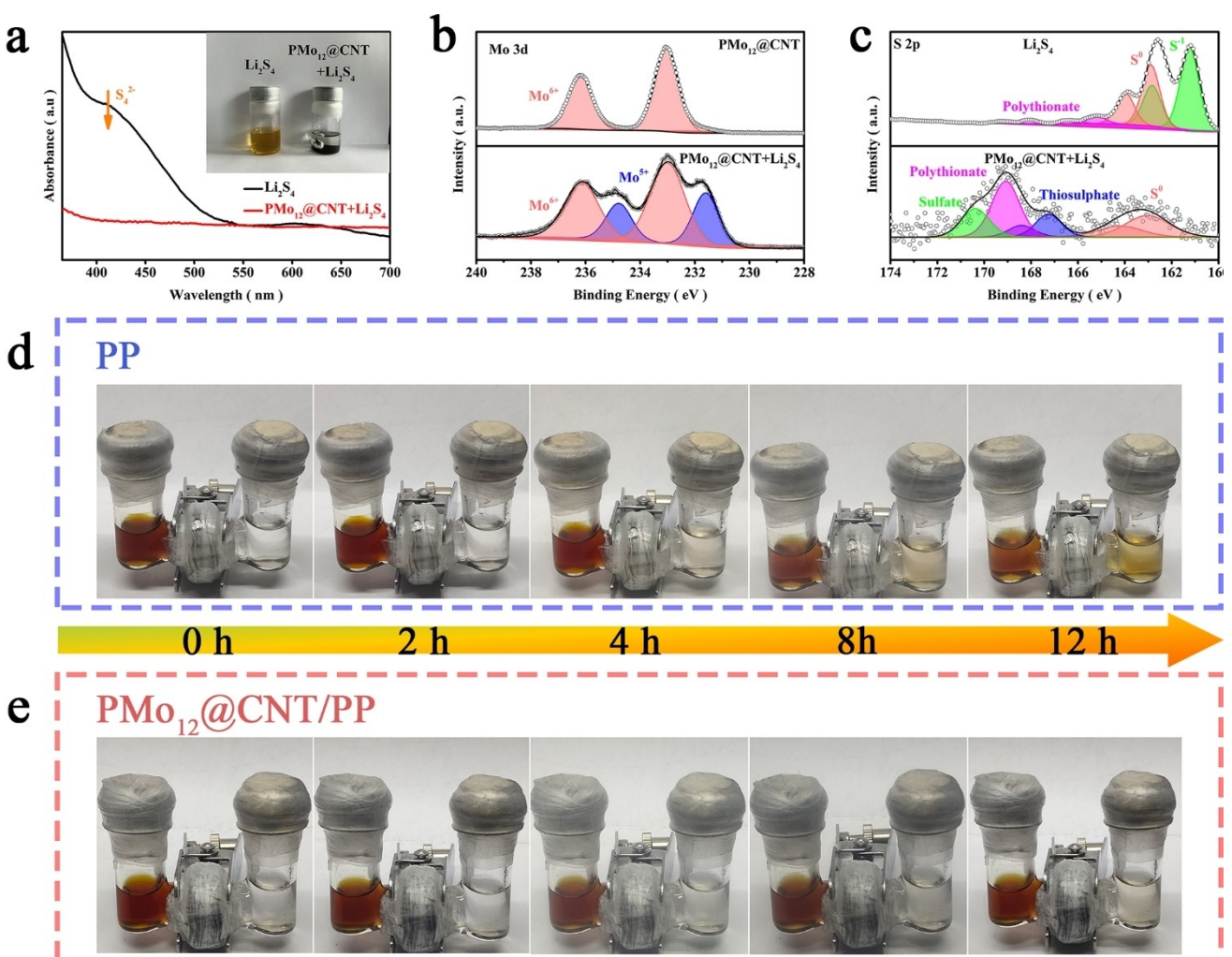


Figure 3. a) Digital pictures and UV vis spectra of Li_2S_4 /DME solution upon contact with blank and $\text{PMo}_{12}\text{@CNT}$; b) Mo 3d XPS spectrum of $\text{PMo}_{12}\text{@CNT}$ clusters and the $\text{PMo}_{12}\text{@CNT}$ clusters after Li_2S_4 treatment; c) S 2p XPS spectrum of Li_2S_4 and the Li_2S_4 after $\text{PMo}_{12}\text{@CNT}$ treatment; d) Digital photograph of a polysulfide diffusion test with a PP and $\text{PMo}_{12}\text{@CNT}/\text{PP}$ separator.

separators. The left cell contained a Li_2S_6 solution, while the right cell contained a standard electrolyte. A PP separator (Figure 3d) and a $\text{PMo}_{12}\text{@CNT/PP}$ separator (Figure 3e) separated the two cells. Due to distinct Li_2S_6 concentrations on both sides, Li_2S_6 spontaneously permeated into the right cell, driven by a high concentration gradient. Upon employing a PP separator, the right side rapidly transitioned from transparency to brown, indicating the penetration of Li_2S_6 through the PP separator. However, with the utilization of the $\text{PMo}_{12}\text{@CNT/PP}$ separator, only a subtle change in color on the right side was observed after 12 h, suggesting a significant reduction in penetration compared to the PP separator. This substantiates the resilient anchoring and catalytic effectiveness of the $\text{PMo}_{12}\text{@CNT/PP}$ separator on Li_2S_6 , successfully hindering the infiltration of LiPSs and alleviating the shuttle effect. To assess the electrocatalytic performance of the $\text{PMo}_{12}\text{@CNT/PP}$ separator in Li–S batteries, a series of electrochemical tests were conducted using both PP and $\text{PMo}_{12}\text{@CNT/PP}$ separators on a dedicated electrochemical workstation. The cyclic voltammetry (CV) curves for the $\text{PMo}_{12}\text{@CNT/PP}$ separator (Figure S5b) exhibit minimal deviation after the initial cycle, and there are no discernible alterations in current or peak positions, revealing better stability and reversibility compared to cells with a PP

separator (Figure S5a). Figure 4a demonstrates the CV curve of the first cycle for both Li–S cells with PP and $\text{PMo}_{12}\text{@CNT/PP}$ separators. The reduction peak at 2.27 V is the reduction of sulfur to soluble intermediate products, whereas the reduction peak at 1.98 V signifies the transition from soluble intermediate products to $\text{Li}_2\text{S}_2/\text{Li}_2\text{S}$ in the CV curve of PP separators. During this process, soluble intermediate products dissolve in the electrolyte, resulting in the reduction of cathode sulfur. The low density of solid $\text{Li}_2\text{S}_2/\text{Li}_2\text{S}$ contributes to volume expansion during charge/discharge. The oxidation peak of the $\text{PMo}_{12}\text{@CNT/PP}$ separator shifts positively by 0.05 V, while the reduction peak shifts negatively by 0.03 V compared to the PP separator, indicating accelerated reaction kinetics of LiPSs. The CV curve of the $\text{PMo}_{12}\text{@CNT}$ electrode reveals multi-electron redox behavior, with a redox potential (E_{eq}) of approximately 2.682 V and 2.753 V vs Li/Li⁺. This voltage range surpasses the redox potential of polysulfides, thereby facilitating the conversion of LiPSs (Figure S6). Electrochemical impedance spectroscopy (EIS) conducted on Li–S cells with different separators reveals a diminished electrolyte/electrode interface resistance ($R_s=1.28 \Omega$) and charge transfer resistance ($R_{\text{ct}}=36.78 \Omega$) for the $\text{PMo}_{12}\text{@CNT/PP}$ separator in contrast to the PP separator ($R_s=5.92 \Omega$, $R_{\text{ct}}=69.59 \Omega$), indicating a reduction in internal

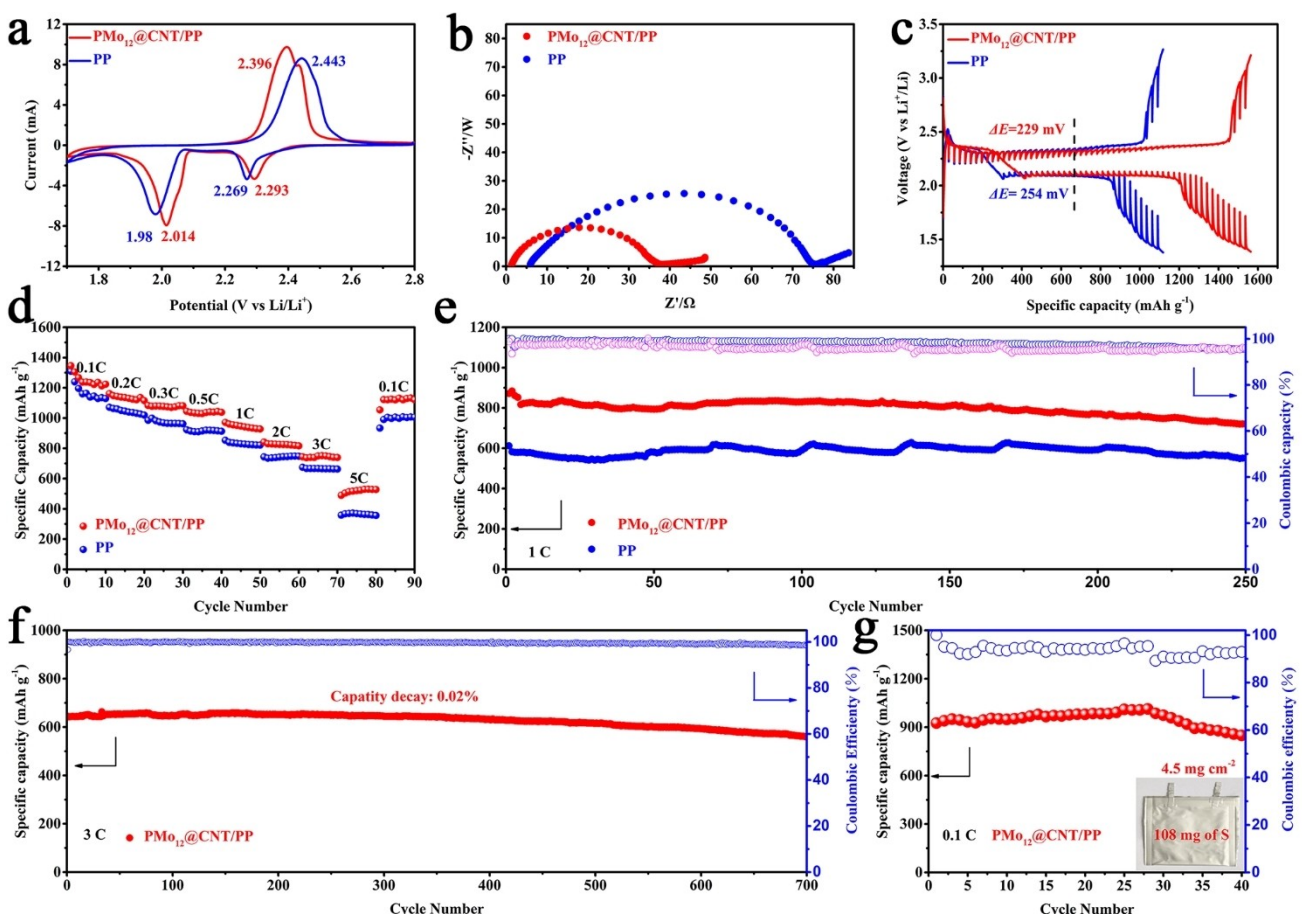


Figure 4. a) CV curve of cell with PP and $\text{PMo}_{12}\text{@CNT/PP}$ separator in the first cycle. b) Nyquist plot of cell with PP and $\text{PMo}_{12}\text{@CNT/PP}$ separator. c) GITT profiles at 0.1 C. d) Rate performance of cell with $\text{PMo}_{12}\text{@CNT/PP}$ and PP separator from 0.1 to 5.0 C. e) Cycling performance and Coulombic efficiency of cell with $\text{PMo}_{12}\text{@CNT/PP}$ and PP separator at 1.0 C. f) Long cycle performance of the cells with $\text{PMo}_{12}\text{@CNT/PP}$ at 3.0 C for 700 cycles. g) Cycling performance of Li–S pouch cell with $\text{PMo}_{12}\text{@CNT/PP}$ separator at 0.1 C.

energy consumption (Figure 4b). The galvanostatic intermittent titration technique (GITT) of Li–S cells with different separators was performed at 0.1 C to investigate the impact of PMo₁₂@CNT/PP on the kinetics of the system throughout the discharge/charging process (Figure 4c). The PMo₁₂@CNT/PP separator consistently demonstrated a smaller overpotential than the PP separator, indicating an enhancement in redox kinetics and a reduction in interfacial reaction barriers. The enhancement observed can be ascribed to the robust catalytic capability of the PMo₁₂ cluster. Furthermore, the PMo₁₂@CNT/PP separator is evaluated using the potentiostatic intermittent titration technique (PITT) to augment Li-ion diffusion in comparison to the PP separator (Figure S7), aligning with the findings from CV.

Galvanostatic charge/discharge at various current rates (Figure 4d) illustrates the superior rate performance of the PMo₁₂@CNT/PP separator, maintaining a high discharge-specific capacity even under elevated current densities. The Li–S cells utilizing the PMo₁₂@CNT/PP separator demonstrated exceptional rate performance, yielding specific capacities of 1346, 1148, 1077, 1037, 960, 830, 737, and 503 mAh g⁻¹ at low rates of 0.1, 0.2, 0.3, 0.5 C, and high rate of 1.0, 2.0, 3.0, and 5.0 C, respectively (Figure S8a, and Figure S8b. This highlights the effectiveness of the PMo₁₂@CNT/PP separator in controlling polysulfide transformation and improving sulfur utilization. In contrast, the PP separator experiences a significant reduction in discharge-specific capacity, especially at high current densities (1.0 C to 5.0 C), attributable to the pronounced shuttle effect of LiPSs. Li–S cells equipped with a PMo₁₂@CNT/PP separator demonstrate a discharge-specific capacity of 852 mAh g⁻¹ at 1.0 C and maintain 715 mAh g⁻¹ after 250 cycles (Figure 4e). The application of the PMo₁₂@CNT/PP separator in Li–S cells yielded notable rate performance and stability (675 mAh g⁻¹ at 3.0 C and 0.02% capacity decay per cycle over 700 cycles), showcasing exceptional capacity retention (Figure 4f). The pouch cell (S:4.5 mg cm⁻²) provides a discharge-specific capacity of 925 mAh g⁻¹ and remains at 849 mAh g⁻¹ after 40 cycles (Figure 4g). Table S1 presents the performance of batteries utilizing the PMo₁₂@CNT/PP separator, offering a comparative analysis with various modified separators.

In a comprehensive investigation of morphological changes in PP, the PMo₁₂@CNT/PP separator, and the lithium metal are characterized using SEM after 250 cycles at 1.0 C. Figure 5a and Figure 5d depict PP and the PMo₁₂@CNT/PP separator after cycling. Relative to their initial states, the uniform holes on the PP separator are predominantly obstructed by lithium LiPSs (Figure 5a). The surface of the PMo₁₂@CNT/PP separator (Figure 5d) exhibits increased roughness and size. Upon removing functional materials from the PMo₁₂@CNT/PP separator, the pores on the PP become visible, and the deposited material does not hinder normal functionality (Figure S9). The initial surface of the lithium metal appears smooth (Figure S10). Nonetheless, in the absence of a barrier, LiPSs traverse the separator, eventually reaching the anode and depositing on the lithium surface after cycling. In contrast, the battery utilizing the PMo₁₂@CNT/PP separator preserves a comparatively smooth lithium metal surface. Furthermore, EDX analysis validates a

reduction in LiPSs shuttling to the anode in batteries equipped with the PMo₁₂@CNT/PP separator (Figure 5b and Figure 5e). The introduction of CNT facilitates the uniform nucleation of Li-ion, stabilizes the lithium anode, and inhibits dendrite formation throughout the entire cycling process. Consequently, the deposited layer of lithium metal in batteries utilizing the PMo₁₂@CNT/PP separator appears thinner after cycling (Figure 5c and Figure 5f). To further validate the protection of the lithium anode by the composite separator, PP and PMo₁₂@CNT/PP separator were employed to assemble a symmetric battery (Li/separator/Li) (Figure 5g). In comparison with the battery equipped with a PP separator, batteries featuring the PMo₁₂@CNT/PP separator exhibit lower overpotential, persisting at only 44 mV after 600 hours of cycles, while the battery with the PP separator is rapidly damaged by dendrites penetrating the separator.

Conclusions

As demonstrated, we devised an innovative bifunctional PMo₁₂@CNT/PP separator to address the challenges of regulating polysulfide transformation and protecting lithium metal in Li–S batteries. The active catalytic properties of PMo₁₂ clusters and the satisfactory physical adsorption capacity of CNT collaboratively capture LiPSs. Leveraging the abundant active sites provided by PMo₁₂ clusters at the electrode/separator interface, LiPSs undergo rapid conversion into the final discharge product, enhancing sulfur utilization and impeding the shuttle effect. Moreover, owing to the commendable electrical conductivity of PMo₁₂@CNT and swift Li-ion conductivity, the PMo₁₂@CNT/PP separator can modulate the Li-ion flux to facilitate Li nucleation. Consequently, the initial battery capacity employing the PMo₁₂@CNT/PP separator was 675 mAh g⁻¹, maintaining 559 mAh g⁻¹ after 700 cycles. The pouch cell (S: 4.5 mg cm⁻²) cycled at 0.1 C exhibited a discharge-specific capacity of 925 mAh g⁻¹ and maintained 849 mAh g⁻¹ after 40 cycles. Additionally, symmetric batteries incorporating the PMo₁₂@CNT/PP separator demonstrate reduced overpotential, maintaining only 44 mV even after 600 hours of cycling. This study investigates the utilization of POMs in lithium-sulfur batteries, anticipating that POMs and their derivatives will find broader applications in Li–S batteries in the future.

Experimental Section

CNT purification

The as-received CNT (Sinopharm, >95%) was purified with a procedure reported by Nakashima et al.^[69] The CNT was placed in a crucible and heated in a tubular furnace at 225 °C for 18 h. The treated CNT was ultrasonic 15 min in hydrochloric acid, then washed with deionized water until pH = 7. The solid material was washed several times with sodium bicarbonate and heated at 50 °C.

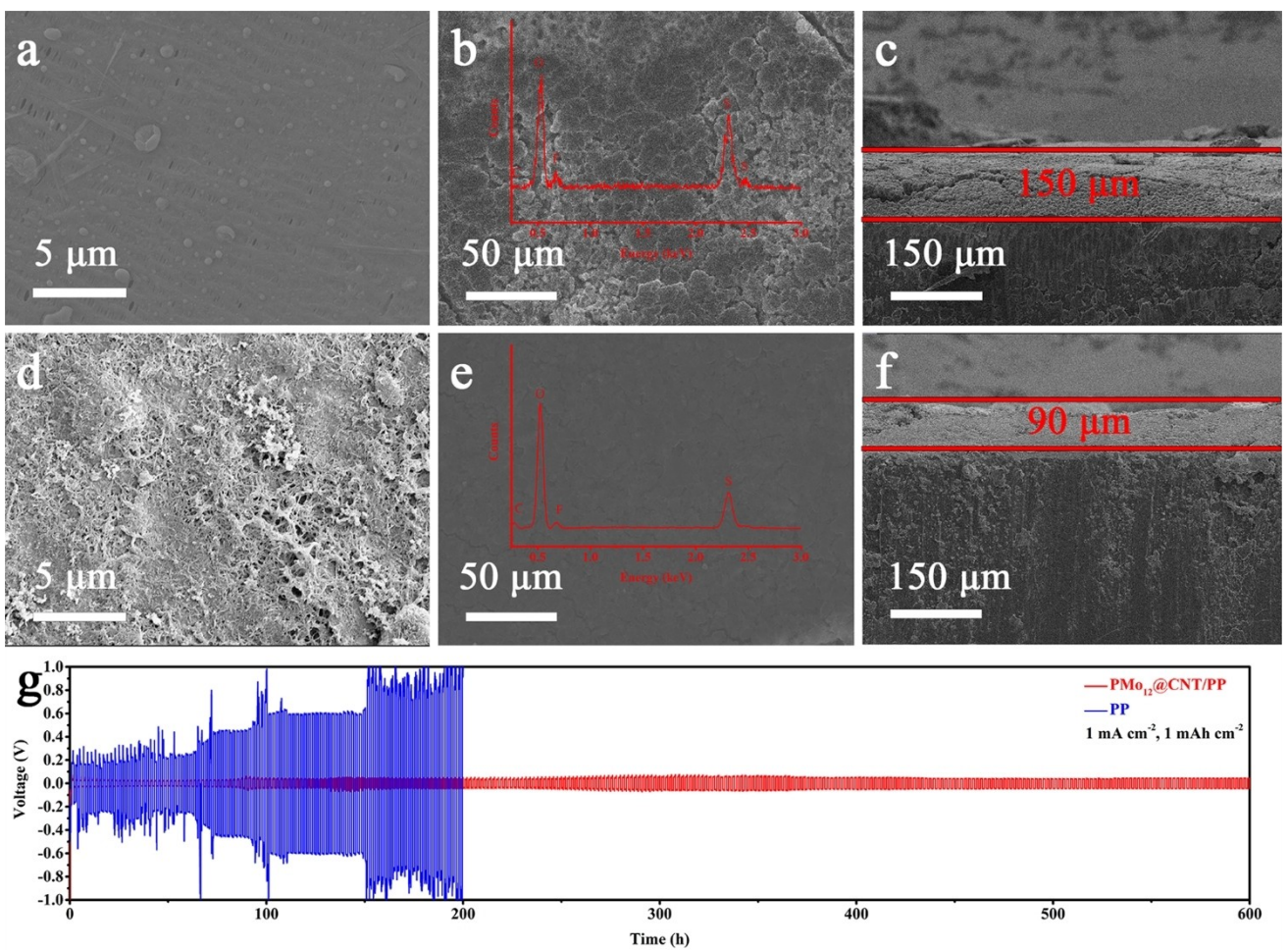


Figure 5. a) SEM images of the PP separator at 1.0 C after 250 cycles. SEM images of the surface b) and cross-section c) of Li metal anode with PP. d) SEM images of PMo₁₂@CNT/PP separator after 250 cycles. Front view e) and cross-section f) of Li metal anode with PMo₁₂@CNT/PP separator; g) Galvanostatic cycling of PP (blue) and PMo₁₂@CNT/PP symmetric battery (red) at 1.0 mA cm⁻².

Synthesis of TBA₃[PMo₁₂O₄₀]

Phosphomolybdic acid (H₃PMo₁₂O₄₀, Sinopharm, AR) and Tetrabutylammonium bromide(TBA, C₁₆H₃₆NBr, Sinopharm, AR) were dissolved in DI water at a molar ratio of 1:3 and reacted in a water bath for 1 h. The yellow precipitate was TBA₃[PMo₁₂O₄₀].

Synthesis of PMo₁₂@CNT

An acetonitrile solution (5 mL) of TBA₃[PMo₁₂O₄₀] (40 mg) was added in CNT (40 mg)-toluene dispersion (50 mL). After stirring the mixture violently at room temperature for 10 minutes and standing for 1 h, the supernatant fluid became colorless, and black precipitation was obtained. The sediment was washed with toluene and dried in a vacuum. The collected material is PMo₁₂@CNT.

Preparation of PMo₁₂@CNT/PP

40 mg PMo₁₂@CNT was uniformly dispersed in 8 mL (10 mg mL⁻¹) PVDF solution, then 40 mL ethanol was added under continuous stirring at room temperature, and ultrasonic stirring for 1 h. 1 mL mixture was dripped on PP (Celgard 2500) via vacuum filtration

until the mixed solution was completely drained. The PMo₁₂@CNT/PP separator was removed and vacuum-dried at 60 °C for 5 h.

Preparation of Li₂S₄/Li₂S₆ solution and polysulfide adsorption

For the synthesis of the Li₂S₄ solution, n(Li₂S):n(S)=1:3 were dissolved in a DOL/DME (1:1 by volume) mixture, and stirred at 80 °C for 7 days. The preparation of the Li₂S₆ solution followed the same procedure as the Li₂S₄ solution, n(Li₂S):n(S)=1:5. Polysulfide adsorption experiments were conducted by adding 20 mg of PMo₁₂@CNT to the Li₂S₄ solution, stirring uniformly for 0.5 h, and standing for several minutes. All procedures were conducted in an argon-filled glovebox.

Visualization of H-tube permeation experiment

A pre-prepared Li₂S₆ solution was introduced to the one side of, and 12 mL of a clear electrolyte was added to the other side. Separate two chambers with PP and PMo₁₂@CNT/PP separator, respectively.

Synthesis of cathode

The cathode slurry comprised a mixture of sulfur/CNT, Super P Li, and polyvinylidene fluoride in a weight ratio of [(7:3);2:1] in N-methyl-pyrrolidone solvent. The cathode slurry was applied to a carbon paper (GDL 28 AA, SGL). The loading of S was \sim 1.2 mg cm $^{-2}$. Furthermore, the ratio of electrolyte to sulfur (E/S) was standardized at 12–15 μ L mg $^{-1}$.

Cell assembly

In the construction of CR2032 coin cells, a meticulously prepared cathode, lithium metal as the anode, and PP and PMo₁₂@CNT/PP as separators, 0.5 M LiCF₃SO₃ and 0.5 M LiNO₃ dissolved in a mixture of DOL/DME (1:1 by volume) as the electrolyte, were utilized. CR2032 coin cells were prepared under an argon atmosphere glove box.

Supporting Information

Supporting Information is available from the Wiley Online Library or the author.

Acknowledgements

This work was supported by the National Natural Science Foundation of China (Nos. 21971221, 21401162, 21773203), the Yangzhou University Interdisciplinary Research Foundation for Chemistry Discipline (yzuxk202010), 'Qing Lan Project' in Colleges and Universities of Jiangsu Province.

Conflict of Interests

The authors declare no conflict of interest.

Data Availability Statement

The data that support the findings of this study are available from the corresponding author upon reasonable request.

Keywords: Lithium-sulfur batteries • Separator • Polyoxometalates • Shuttle effect • Lithium dendrite

- [1] S. J. Fretz, M. Agostini, P. Jankowski, P. Johansson, A. Matic, A. E. C. Palmqvist, *Batteries & Supercaps* 2020, 3, 757–765.
- [2] A. Manthiram, Y. Fu, S. Chung, C. Zu, Y. S. Su, *Chem. Rev.* 2014, 114, 11751–11787.
- [3] S. Zhang, M. Zheng, Z. Lin, R. Zang, Q. Huang, H. Xue, J. Cao, H. Pang, *RSC Adv.* 2016, 6, 39918–39925.
- [4] L. Ni, S. Duan, H. Zhang, J. Gu, G. Zhao, Z. Lv, G. Yang, Z. Ma, Y. Liu, Y. Fu, Z. Wu, J. Xie, M. Chen, G. Diao, *Carbon* 2021, 182, 335–347.
- [5] X. Liu, J. Huang, Q. Zhang, L. Mai, *Adv. Mater.* 2017, 29, 1601759.
- [6] L. Sun, K. Li, J. Fu, B. Tian, C. Wang, H. Li, L. Wang, *Inorg. Chem.* 2021, 60, 12847–12854.
- [7] G. Di Donato, T. Ates, H. Adenusi, A. Varzi, M. A. Navarra, S. Passerini, *Batteries & Supercaps* 2022, 5, e202200097.
- [8] Z. Li, J. T. Zhang, Y. M. Chen, J. Li, X. W. Lou, *Nat. Commun.* 2015, 6, 8850.

- [9] T. S. Sahu, S. Choi, P. Jaumaux, J. Zhang, C. Wang, D. Zhou, G. Wang, *Polyhedron* 2019, 162, 147–154.
- [10] X. Liang, C. Y. Kwok, F. Lodi-Marzano, Q. Pang, M. Cuisinier, H. Huang, C. J. Hart, D. Houtarde, K. Kaup, H. Sommer, T. Brezesinski, J. Janek, L. F. Nazar, *Adv. Energy Mater.* 2016, 6, 1501636.
- [11] R. Xiao, S. Yang, T. Yu, T. Hu, X. Zhang, R. Xu, Y. Wang, X. Guo, Z. Sun, F. Li, *Batteries & Supercaps* 2022, 5, 202100389.
- [12] Z. A. Ghazi, X. He, A. M. Khattak, N. A. Khan, B. Liang, A. Iqbal, J. Wang, H. Sin, L. Li, Z. Tang, *Adv. Mater.* 2017, 29, 1606817.
- [13] P. Zhu, J. Zhu, J. Zang, C. Chen, Y. Lu, M. Jiang, C. Yan, M. Dirican, R. K. Selvan, X. Zhang, *J. Mater. Chem. A* 2017, 5, 15096–15104.
- [14] M. Du, P. Geng, C. Pei, X. Jiang, Y. Shan, W. Hu, L. Ni, H. Pang, *Angew. Chem. Int. Ed.* 2022, 61, e202209350.
- [15] F. Ma, Z. Chen, K. Srinivas, D. Liu, Z. Zhang, Y. Wu, M. Zhu, Q. Wu, Y. Chen, *Chem. Eng. J.* 2023, 459, 141526.
- [16] S. Maletti, F. S. Podetti, S. Oswald, L. Giebel, C. A. Barbero, D. Mikhailova, J. Balach, *ACS Appl. Energ. Mater.* 2020, 3, 2893–2899.
- [17] T. Zhuang, J. Huang, H. Peng, L. He, X. Cheng, C. Chen, Q. Zhang, *Small* 2016, 12, 381–389.
- [18] F. Pei, L. Lin, A. Fu, S. Mo, D. Ou, X. Fang, N. Zheng, *Joule* 2018, 2, 323–336.
- [19] L. Zhang, Y. Wang, Z. Niu, J. Chen, *Carbon* 2019, 141, 400–416.
- [20] S. Yang, Y. Cheng, X. Xiao, H. Pang, *Chem. Eng. J.* 2020, 384, 123294.
- [21] X. Jiang, Y. Chen, X. Meng, W. Cao, C. Liu, Q. Huang, N. Naik, V. Murugadoss, M. Huang, Z. Guo, *Carbon* 2022, 191, 448–470.
- [22] Y. Han, C. Qian, H. Wu, X. Chen, X. Wu, W. He, H. Yan, G. Li, G. Diao, M. Chen, *J. Energy Chem.* 2021, 54, 761–769.
- [23] X. Wu, H. Wu, B. Xie, R. Wang, J. Wang, D. Wang, Q. Shi, G. Diao, M. Chen, *ACS Nano* 2021, 15, 14125–14136.
- [24] H. Wu, N. Xu, Z. Jiang, A. Zheng, Q. Shi, R. Lv, L. Ni, G. Diao, M. Chen, *Chem. Eng. J.* 2022, 427, 131002.
- [25] W. Wang, Y. Tao, J. Fan, Z. Yan, H. Shang, D. L. Phillips, M. Chen, G. Li, *Adv. Funct. Mater.* 2022, 32, 2201357.
- [26] Y. Xie, S. Zong, L. Lu, K. Zhang, *Polyhedron* 2022, 226, 116095.
- [27] Y. Chen, W. Qi, K. Zhang, *Dalton Trans.* 2023, 52, 5687–5703.
- [28] N. Li, X. Ma, H. Ye, S. Wang, K. Han, *J. Phys. Chem. Solids* 2019, 134, 69–76.
- [29] S. Ji, S. K. Kim, S. H. Choi, J. S. Byun, D. K. Kim, H. J. Lee, H. M. Choi, W. Song, S. Myung, J. Suk, K.-S. An, S. S. Lee, *ACS Appl. Energ. Mater.* 2022, 5, 12196–12205.
- [30] Y. Wu, N. Wu, X. Jiang, S. Duan, T. Li, Q. Zhou, M. Chen, G. Diao, Z. Wu, L. Ni, *Inorg. Chem.* 2023, 62, 15440–15449.
- [31] J. Huang, T. Zhuang, Q. Zhang, H. Peng, C. Chen, F. Wei, *ACS Nano* 2015, 9, 3002–3011.
- [32] Z. Zhang, Y. Lai, Z. Zhang, K. Zhang, J. Li, *Electrochim. Acta* 2014, 129, 55–61.
- [33] J. He, Y. Chen, A. Manthiram, *Energy Environ. Sci.* 2018, 11, 2560–2568.
- [34] N. Li, Y. Xie, S. Peng, X. Xiong, K. Han, *J. Energy Chem.* 2020, 42, 116–125.
- [35] S. Bai, X. Liu, K. Zhu, S. Wu, H. Zhou, *Nat. Energy* 2016, 1, 16094.
- [36] K. Li, Y. Liu, X. Lin, G. Yang, *Inorg. Chem.* 2022, 61, 6934–6942.
- [37] G. Yang, X. Xie, M. Cheng, X. Gao, X. Lin, K. Li, Y. Cheng, Y. Liu, *Chin. Chem. Lett.* 2022, 33, 1483–1487.
- [38] Z. Ni, N. L, C. Z, L. Mi, *Polyoxometalates* 2023, 3, 9140044.
- [39] D. Z, H. W, *Polyoxometalates* 2022, 1, 9140006.
- [40] L. Ni, H. Xu, H. Li, H. Zhao, G. Diao, *Polyhedron* 2018, 155, 59–65.
- [41] J. K. Hurst, *Science* 2010, 328, 315–316.
- [42] L. Zhang, T. Li, X. Zhang, Z. Ma, Q. Zhou, Y. Liu, X. Jiang, H. Zhang, L. Ni, G. Diao, *J. Mater. Chem. A* 2023, 11, 3105–3117.
- [43] J. Li, Y. Wang, C. Liu, S. Li, Y. Wang, L. Dong, Z. Dai, Y. Li, Y. Lan, *Nat. Commun.* 2016, 7, 11204.
- [44] P. Wang, H. Zhang, P. Wang, J. Zha, J. Gautam, H. Zhang, R. Li, L.-n. Zhang, G. Diao, L. Ni, *Catal. Commun.* 2022, 165, 106446.
- [45] Y. Liu, S. Liu, D. He, N. Li, Y. Ji, Z. Zheng, F. Luo, S. Liu, Z. Shi, C. Hu, *J. Am. Chem. Soc.* 2015, 137, 12697–12703.
- [46] H. Zhang, Z. Ma, S. Duan, Y. Liu, X. Jiang, Q. Zhou, M. Chen, L. Ni, G. Diao, *Electrochim. Acta* 2022, 428, 140868.
- [47] I. A. Weinstock, R. E. Schreiber, R. Neumann, *Chem. Rev.* 2018, 118, 2680–2717.
- [48] Y. Wei, *Polyoxometalates* 2022, 1, 9140014.
- [49] H. Zhang, H. Zhao, W. Chang, X. Liu, P. Chen, A. Yu, A. N. Chishti, Y. Zhang, L. Ni, X. Wang, Y. Wei, *Tungsten* 2023, 5, 225–234.
- [50] G. Yang, Y. Wu, Z. Lv, X. Jiang, J. Shi, Y. Zhang, M. Chen, L. Ni, G. Diao, Y. Wei, *Chem. Commun.* 2023, 59, 788–791.

- [51] P. Wang, A. N. Chishti, P. Chen, Z. Lv, Y. Tan, H. Zhang, J. Zha, Z. Ma, L. Ni, L. Zhang, Y. Wei, *CrystEngComm* **2022**, *24*, 8134–8140.
- [52] Y. Huang, J. Ge, J. Hu, J. Zhang, J. Hao, Y. Wei, *Adv. Energy Mater.* **2018**, *8*, 1701601.
- [53] Y. Wang, Y. Lu, W. Zhang, T. Dang, Y. Yang, X. Bai, S. Liu, *Polyoxometalates* **2022**, *1*, 9140005.
- [54] D. Long, R. Tsunashima, L. Cronin, *Angew. Chem. Int. Ed.* **2010**, *49*, 1736–1758.
- [55] Q. Zhou, X. Zhang, Y. Wu, X. Jiang, T. Li, M. Chen, L. Ni, G. Diao, *Small* **2023**, 202304515.
- [56] S. Wang, G. Yang, *Chem. Rev.* **2015**, *115*, 4893–4962.
- [57] L. Ni, H. Li, H. Xu, C. Shen, R. Liu, J. Xie, F. Zhang, C. Chen, H. Zhao, T. Zuo, G. Diao, *ACS Appl. Mater. Interfaces* **2019**, *11*, 38708–38718.
- [58] L. Ni, G. Yang, C. Sun, G. Niu, Z. Wu, C. Chen, X. Gong, C. Zhou, G. Zhao, J. Gu, W. Ji, X. Huo, M. Chen, G. Diao, *Mater. Today Energy* **2017**, *6*, 53–64.
- [59] J. C. Ye, J. J. Chen, R. M. Yuan, D. R. Deng, M. S. Zheng, L. Cronin, Q. F. Dong, *J. Am. Chem. Soc.* **2018**, *140*, 3134–3138.
- [60] L. Ni, G. Yang, Y. Liu, Z. Wu, Z. Ma, C. Shen, Z. Lv, Q. Wang, X. Gong, J. Xie, G. Diao, Y. Wei, *ACS Nano* **2021**, *15*, 12222–12236.
- [61] J. Lei, X. Fan, T. Liu, P. Xu, Q. Hou, K. Li, R. Yuan, M. Zheng, Q. Dong, J. Chen, *Nat. Commun.* **2022**, *13*, 202.
- [62] W. Yao, L. Liu, X. Wu, C. Qin, H. Xie, Z. Su, *ACS Appl. Mater. Interfaces* **2018**, *10*, 35911–35918.
- [63] L. Ni, J. Gu, X. Jiang, H. Xu, Z. Wu, Y. Wu, Y. Liu, J. Xie, Y. Wei, G. Diao, *Angew. Chem. Int. Ed.* **2023**, *62*, 202306528.
- [64] H. Hu, X. Jia, J. Wang, W. Chen, L. He, Y. Song, *Inorg. Chem. Front.* **2021**, *8*, 352–360.
- [65] R. Abazari, L. Esrafilii, A. Morsali, Y. Wu, J. Gao, *Appl. Catal. B* **2021**, *283*, 119582.
- [66] D. Hu, X. Song, S. Wu, X. Yang, H. Zhang, X. Chang, M. Jia, *Chin. J. Catal.* **2021**, *42*, 356–366.
- [67] C. Zheng, N. Luo, S. Huang, W. Wu, H. Huang, M. Wei, *ACS Sustainable Chem. Eng.* **2019**, *7*, 10198–10206.
- [68] L. Ni, Z. Wu, G. Zhao, C. Sun, C. Zhou, X. Gong, G. Diao, *Small* **2017**, *13*, 201603466.
- [69] U. Kortz, S. Isber, M. H. Dickman, D. Ravot, *Inorg. Chem.* **2000**, *39*, 2915–2922.

Manuscript received: November 30, 2023

Revised manuscript received: January 2, 2024

Version of record online: January 19, 2024
